Unveiling Oxygen Redox Activity in P2-Type NaxNi0.25Mn0.68O2 High-Energy Cathode for Na-Ion Batteries

Publisher copyright

(Article begins on next page)

12 September 2024

LETTER

Unveiling Oxygen Redox Activity in P2-Type Na$_x$Ni$_{0.25}$Mn$_{0.68}$O$_2$ High-Energy Cathode for Na-Ion Batteries

Arianna Massaro, Ana B. Muñoz-García,* Pier Paolo Prosini, Claudio Gerbaldi, and Michele Pavone*

ACCESS | 📊 Metrics & More | 📖 Article Recommendations | 🔒 Supporting Information

ABSTRACT: Na-ion batteries are emerging as convenient energy-storage devices for large-scale applications. Enhanced energy density and cycling stability are key in the optimization of functional cathode materials such as P2-type layered transition metal oxides. High operating voltage can be achieved by enabling anionic reactions, but irreversibility of O^{2-}/O$_2^{n-}$/O$_2$ evolution still limits this chance, leading to extra capacity at first cycle that is not fully recovered. Here, we dissect this intriguing oxygen redox activity in Mn-deficient Na$_x$Ni$_{0.25}$Mn$_{0.68}$O$_2$ from first-principles, by analyzing the formation of oxygen vacancies and dioxygen complexes at different stages of sodiation. We identify low-energy intermediates that release molecular O$_2$ at high voltage, and we show how to improve the overall cathode stability by partial substitution of Ni with Fe. These new atomistic insights on O$_2$ formation mechanism set solid scientific foundations for inhibition and control of this process toward the rational design of new anionic redox-active cathode materials.
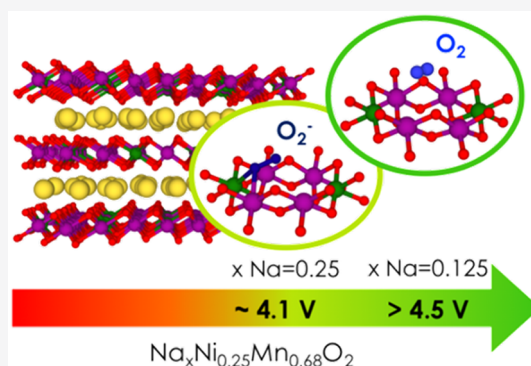
Electrical energy storage (EES) is key for an effective use of renewable sources with intermittent nature. The urgent need for a sustainable world economy is pushing the production and deployment of large-scale EES systems and their integration into smart electrical grids.[1,2] Since the breakthrough of Li-ion battery (LIB) technology, extensive research in both academia and industry has been focusing on alternative chemistries based on cheaper and widespread resources (e.g., sodium- or magnesium-based batteries).[3−6] When fabricated in all-solid-state configuration, Na-ion batteries (NIBs) meet the cost and safety requirements that are essential for their deployment in the market.[7,8] Inspired by working principles similar to LIBs, significant efforts have been devoted to the design of efficient NIB component materials starting from electrodes and electrolytes of Li-based cells.[9] However, the differences between Li$^+$ and Na$^+$ ions (e.g., electrochemical potential, ionic radius) have revealed that, in most cases, sodium-analogues of state-of-the-art LIB materials do not represent a satisfactory solution. Thus, the consolidation of NIB technology relies on enhanced energy density and stability to be achieved via high-performing Na$^+$ host materials and safe Na$^+$ conductors.[10−12] Within this framework, the development of high-energy and structurally stable NIB positive electrodes operating at voltage values in the order of 4.5 V (or even above) represents a current *Grand Challenge*

because it is the cathode that mainly affects the battery performance and manufacturing costs. Among several explored materials, layered transition metal (TM) oxides, Na$_x$TMO$_2$ (0 < x < 1), have attracted special attention thanks to their easy synthesis and promising electrochemical performances.[13−16] Similar to the Li$_x$TMO$_2$ counterpart, the crystalline structure alternates planar layers of alkali metal ions and edge-sharing TMO$_6$ octahedra, where Na ions can easily move in and out upon cycling, with the charge being compensated by the reversible reduction and oxidation of TM ions. Na$_x$TMO$_2$ can crystallize in either O3- or P2-polymorphs, which differ in the symmetry at the Na site (octahedral O or prismatic P) and the number of TMO$_2$-layers in the unit cell (three layers with "ABC" scheme for oxygen stacking in the O3- packing or two layers with "ABBA" sequence in the P2- one).[17] P2-type phases usually exhibit excellent reversible capacity and superior rate performance compared with O3- ones, thanks to a higher Na$^+$ mobility enabled by the open prismatic diffusion pathways and
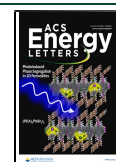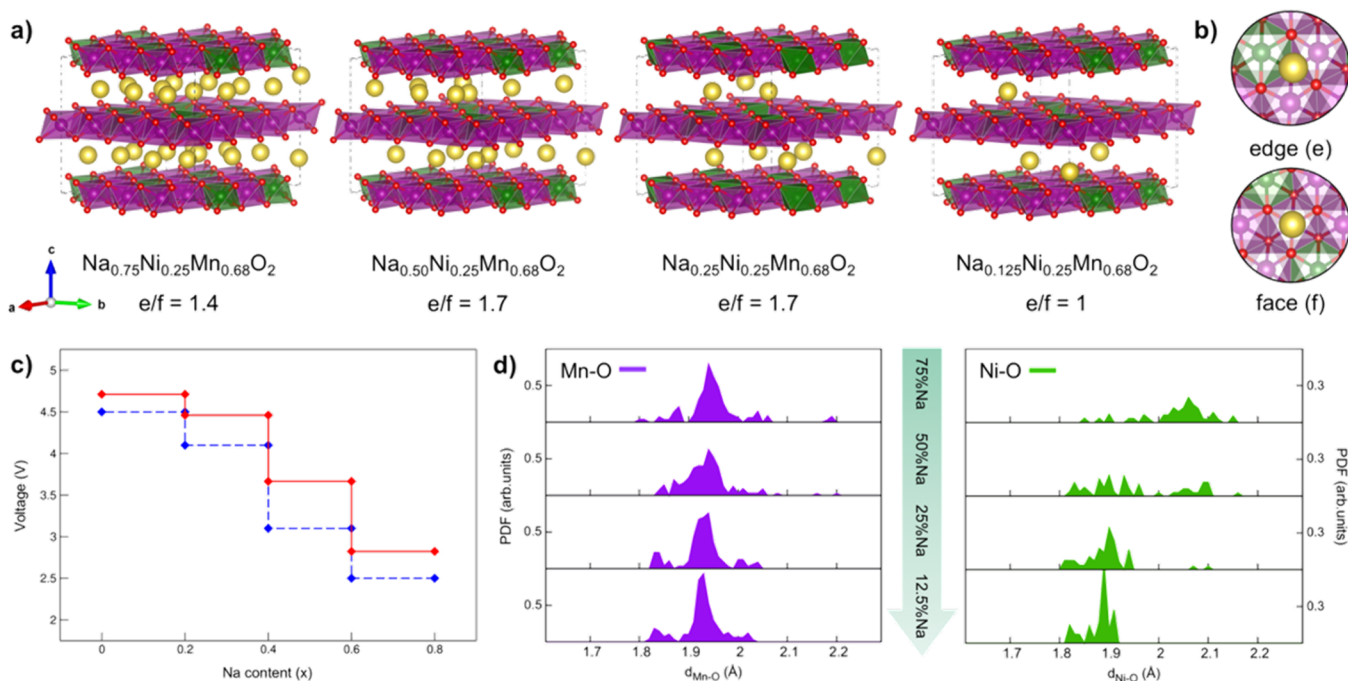
Figure 1. (a) Minimum-energy structures of NNMO systems obtained at the PBE+U(-D3BJ) level of theory. Atoms are represented as spheres and coordination octahedra at the TM (TM = Mn, Ni) sites are highlighted. Color code: Na, yellow; Ni, green; Mn, purple; O, red. Values of e/f ratio after relaxation are reported. (b) Coordination details of both edge and face Na sites. (c) Computed capacity-voltage plot of NNMO (red solid lines) in comparison to experimental-derived data taken from ref 20 (blue dashed lines). (d) PDF of Mn−O (purple) and Ni−O (green) distances in NNMO computed at the PBE+U(-D3BJ) level of theory.

higher Na content, which allows larger specific capacity and improved stability.[18−20] However, a simple gliding of TMO$_2$ sheets with no breaking of M−O bonds can occur upon electrochemical cycling, leading to an undesired P2−O2 phase transitions and related instability issues.[21,22] For certain compositions, for example Fe-containing TMO$_2$, even very complex P2−O2 phase transitions have been reported at high operating voltage, involving dynamically changing intergrowth structures called "Z"-phase.[23,24]

Among all TMs layered oxides, many studies focus on Mn because it promises reduced costs, increased sustainability, and improved performance.[25] One of the most exploited approaches to retain the P2 structure upon cycling consists in playing ion substitutions at the Mn site by doping with a variety of metal ions (e.g., Li$^+$, Mg^{2+}, Ti^{4+}, Fe^{2+}, Co^{2+}, Ni^{2+}, Cu^{2+}, Zn^{2+}), which can affect the phase stability and thus the overall cell efficiency.[23,26−34] For example, it has been shown that the substitution of inert alkali metals, such as potassium, at the Na site in Na$_x$TMO$_2$ allows to uphold the layer-structured framework upon cycling and thus improve the overall cycle life.[35] Remarkably, recent works suggested that high energy density in both LIBs and NIBs can be attained via an additional redox activity, that is, the charge being stored not only by the TM but also by the oxide sublattice.[16,36−40] In this way, the theoretical specific capacity goes beyond the fixed limits of TM redox potentials, leading to a new paradigm in research and development of advanced cathode materials. Experimental evidence of oxygen participation to charge compensation upon delithiation in LIBs is extensively reported,[41−46] and its correlation with high Li content has been elucidated from *ab initio* calculations:[47] in alkali-rich layered oxides, some oxygen atoms are coordinated by two TMs, thus showing just below the Fermi level a nonbonding 2p

oxygen orbital, which can directly participate in the oxidation process. These findings have suggested an optimization strategy based on alkali metal ion substitutions at the TM Wyckoff sites, but it has been observed that the metal migrates upon cycling, with detrimental effects on overall performances.[48,49] Introducing a TM vacancy emerged as another possible approach, leading to similar 2p nonbonding orbital on oxygen atoms and, at the same time, keeping the TM migration suppressed.[20,50] TM-deficient layers feature Na−O−TM vacancy configurations that can act as highly ionic sites where electron holes on O atoms can be stabilized, and thus, the anionic activity can be triggered.[42,47,51] Whether these materials can accomplish a fully reversible O-redox process or undergo O$_2$ loss still remains an open question.[19,20]

Recently, the first-cycle voltage hysteresis observed during galvanostatic cycling of Na-based high-energy cathodes has been associated with cation ordering at the superstructure level, suggesting that specific arrangements can drive the stabilization of oxygen electron holes and preserve the O-redox activity upon subsequent cycling.[36,52] However, an in-depth investigation on these charge compensation mechanisms is still missing. Indeed, increasing efforts are devoted to assess the structure−property−function relationships in these promising NIB electrode materials and to find suitable descriptors that are able to correlate their chemical compositions and electrochemical performances.[53] With these aims, computational modeling offers the atomistic perspective needed to assist experiments in elucidating the details of O-based redox processes and the effects of point defects on the related mechanisms. The success of *in silico* experiments is well-established in this research area as rational strategies are fundamental toward the design of highly performing sodium intercalation electrodes for advanced Na-ion batteries.[54−56]
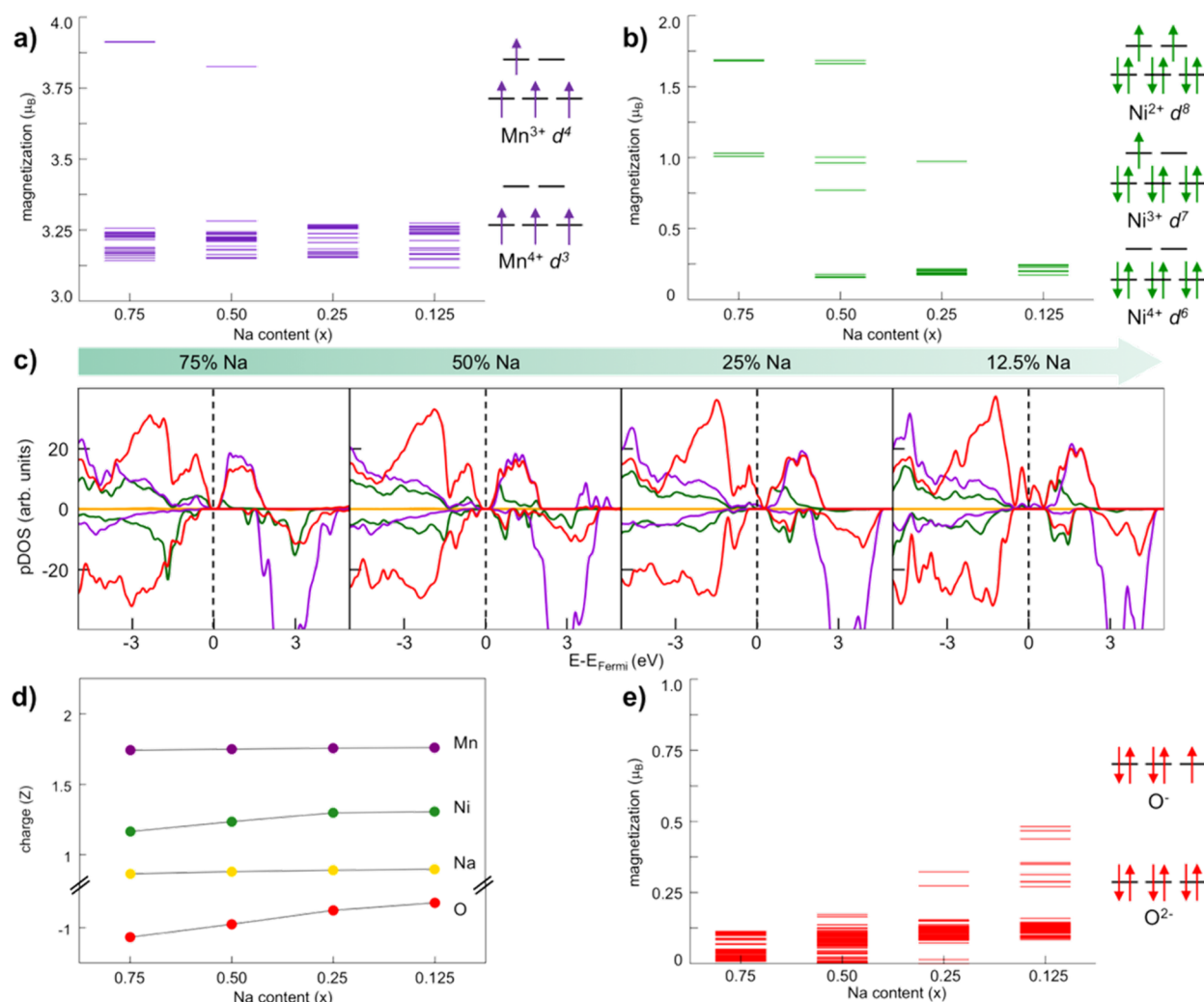
Figure 2. Electronic structure analysis of NNMO as a function of Na content: net magnetic moments on Mn (a) and Ni (b) species, with the corresponding electronic configuration on the side; (c) atom- and angular momentum- pDOS computed at the PBE+U(-D3BJ) level of theory; (d) Bader charge analysis reported as the average charge for each element; (e) net magnetic moment on O atoms with corresponding electronic configuration on the side. Color code: Na s states, yellow; Mn d states, purple; Ni d states, green; O p states, red.

Within this context, here we report a first-principles study of the P2-type Mn-deficient layered oxide with formula $Na_xNi_{0.25}Mn_{0.68}O_2$ (NNMO). This material exhibits outstanding electrochemical performance for rechargeable NIBs.[20] From EELS and sXAS experiments, the electrochemically cycled NNMO particles show a gradient of TM oxidation states that is ascribed to the loss of oxygen,[20] a novel electrochemical feature also found in other similar high-energy NIB cathodes. The presence of Mn vacancies is shown to be beneficial for the cathode performances and is considered to be responsible for the O-redox activation.[20] For this reason, the focus of our study is the Mn-deficient $Na_xNi_{0.25}Mn_{0.68}O_2$ phase. We aim at dissecting this NNMO feature at the atomistic level and from first-principles to determine the O-redox activity at different sodiation stages, while concurrently providing new insights on the underlying mechanisms.

The minimum-energy structures for NNMO systems obtained at the PBE+U(-D3BJ) level of theory are reported in Figure 1a. We have employed the special quasi random approach (SQS), a state-of-the-art method to study solid solutions with two or more components.[57−60] The SQS models would allow our NNMO local minimum-energy

structures to account for the configurational entropy properly. The relative Na occupancies at edge/face (e/f) sites (Figure 1b) change in the Mn-deficient systems (e/f ratio values turn out to be lower than 2), showing a stabilization of face sites over edge ones in NNMO compared to the $Na_xNi_{0.25}Mn_{0.75}O_2$ counterpart (see Figure S1 in SI for comparison). The DFT+U scheme is widely adopted to investigate structural and electronic features of transition metal oxides.[61−64] Lately, several studies focusing on similar layered Na_xTMO_2 as cathode materials have shown that the PBE+U approach allows to reach good accuracy with affordable computational costs.[35,37,38,65] We have computed the intercalation potential values for each sodiation state according to eq 1:

$$V = -\frac{E_{Na_{x_2}NNMO} - E_{Na_{x_1}NNMO} - (x_2 - x_1)\frac{1}{2}E_{Na}}{(x_2 - x_1)} \quad (1)$$

where $E_{Na_{x_2}NNMO}$ and $E_{Na_{x_1}NNMO}$ are the total energies of NNMO at, respectively, x_2 and x_1 Na composition ($x_1 < x_2$), E_{Na} is the total energy of sodium metal considering the bcc lattice with 2 atoms in the unit cell.[54] The corresponding computed capacity-voltage profile (red profile in Figure 1c) is

in qualitative agreement with intercalation potentials derived from the available experimental data (blue profile in Figure 1c), thus confirming the reliability of our model.[20] We have analyzed the structural properties along the desodiation process by calculating the pair distribution function (PDF) of Mn−O and Ni−O distances, as shown in Figure 1d. While the Mn−O distance pattern is almost identical for each sodiation degree (with an average value of ∼1.9 Å), Ni−O bonds undergo a significant shortening with decreasing Na content (the highest peak shifting from ∼2.1 Å to ∼1.8 Å), which is even more pronounced than in the stoichiometric $Na_xNi_{0.25}Mn_{0.75}O_2$ case (Figure S2 in SI).

Analysis of the electronic structure clarifies the origin of these structural features. The magnetization of each Mn and Ni atom, plotted against Na content (panels a and b, respectively, of Figure 2), reveals that desodiation induces $Ni^{2+} \rightarrow Ni^{3+} \rightarrow Ni^{4+}$ oxidation, while Mn^{4+} oxidation state is essentially retained. This is in agreement with previous spectroscopic measurements performed on similar $Na_xNi_yMn_{1-y}O_2$ cathode materials.[20,40] Other Mn oxidation states (Mn^{3+}, Mn^{2+}) detected on the surface of cycled NNMO samples are attributed to O vacancies,[20] or to detrimental electrolyte decomposition occurring at the cathode/electrolyte interface.[40] As a matter of fact, alternative ionic liquid-based electrolytes are shown to effectively improve the cycling stability.[40] In any case, such variations are not related to the sodiation/desodiation process. We must note that, in this material, real charges are far from the ionic limit, as a result of the high covalent character of TM-O bonds, because of the strong hybridization of TM d states with O p ones. This feature is evinced by the projected density of states (pDOS) reported in Figure 2c. That being said, oxidation state variation trends upon desodiation are confirmed by the constant/increasing Bader charges for Mn/Ni species, respectively (Figure 2d). Figure 2e shows the trend of magnetization at O sites, which increases to ∼0.3 μ_B at $x = 0.25$ and up to ∼0.5 μ_B at $x = 0.125$, indicating a partial oxidation of O^{2-} species. The formation of electron holes on oxygen atoms can be also identified from the pDOS, where O p states in the valence band cross the Fermi level, leading to a p-type character at $x = 0.25$ and 0.125. Our findings are in close agreement to recent DFT and XAS results by Zhao et al. for the closely related $Na_{10-x}LiNi_3Mn_8O_{24}$ layered oxide, which indicate electron extraction taking place from Ni 3d states upon charge, and O 2p states starting to participate at high desodiation degrees.[19]

In order to explore the O-redox activity in NNMO, we first address the thermodynamics of oxygen vacancy (V_O) formation. The removal of one oxygen atom in our 4 × 4 × 1 supercell corresponds to 1.56% of V_O concentration, which is in agreement with experimental records from a Li-based analogue.[66] As shown in Figure 3a, four types of vacancies have been considered, differing for both the coordination to the Mn-deficient site (first or second coordination shell, V_O (1) and V_O (2), respectively) and the chemical environment (Mn−O−Mn or Mn−O−Ni, V_O (a) and V_O (b), respectively). The V_O formation energy, E_{V_O}, has been computed according to eq 2:

$$E_{V_O} = E_{def} - E_{prist} + \frac{1}{2}E_{O_2} \qquad (2)$$

where E_{def} and E_{prist} are the total energies of O-defective and pristine NNMO, respectively, and E_{O_2} is the total energy of the
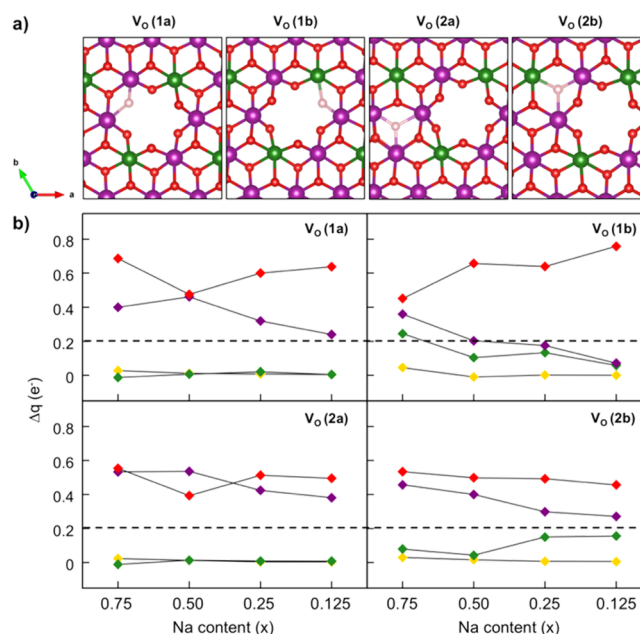

Figure 3. (a) Optimized structures of different kind of oxygen vacancies considered in the present work. In pink, the original position of the leaving oxygen. (b) Cumulative charge variation upon vacancy formation, $\Delta q = q_{def} - q_{prist}$, for each element sublattice plotted for each sodiation state. Color code: Na, yellow; Ni, green; Mn, purple; O, red. The black dashed lines at threshold $\Delta q = 0.2e^-$ are included as guideline for the eyes for an easier identification of significant charge variations.

oxygen molecule as computed in its triplet ground state. Calculated values for each nonequivalent V_O at each Na content are listed in Table 1.

Table 1. Oxygen Vacancy Formation Energies (in eV) Computed at the PBE+U(-D3BJ) Level of Theory According to eq 2[a]

x Na	V_O (1a)	V_O (1b)	V_O (2a)	V_O (2b)
0.75	1.866	2.623	3.204	3.443
0.50	1.944	1.447	2.865	2.858
0.25	1.515	1.079	2.454	2.587
0.125	1.077	0.114	2.537	2.390

[a]Labels of O-vacancies according to Figure 3a.

These results show that (1) oxygen vacancies are more likely to occur next to the Mn-deficient site rather than in the second coordination shell, as it is easier to remove a two-coordinated oxygen atom than a three-coordinated one ($E_{V_O(1*)} < E_{V_O(2*)}$). Indeed, $V_O(1)$-like vacancies are also more stable than three-coordinated V_O ones in the stoichiometric phase (see Table S1). (2) There is a general trend of decreasing formation energy upon desodiation because of charge compensation effects, leading to more favorable accommodation of reducing defects (V_O) in oxidized states (desodiated structures). (3) Mn−V_O−Ni configurations are more convenient than Mn−V_O−Mn ones, as a result of the higher lability of the involved M−O bonds ($E_{V_O(*b)} < E_{V_O(*a)}$). Even at low Na contents, breaking the Ni−O bond is still more favorable than breaking a Mn−O one, since the excess charge mostly delocalizes on the whole O sublattice (see corresponding panels in Figure 3b), leading to a significant defect stabilization.[67,68] (4) Lower
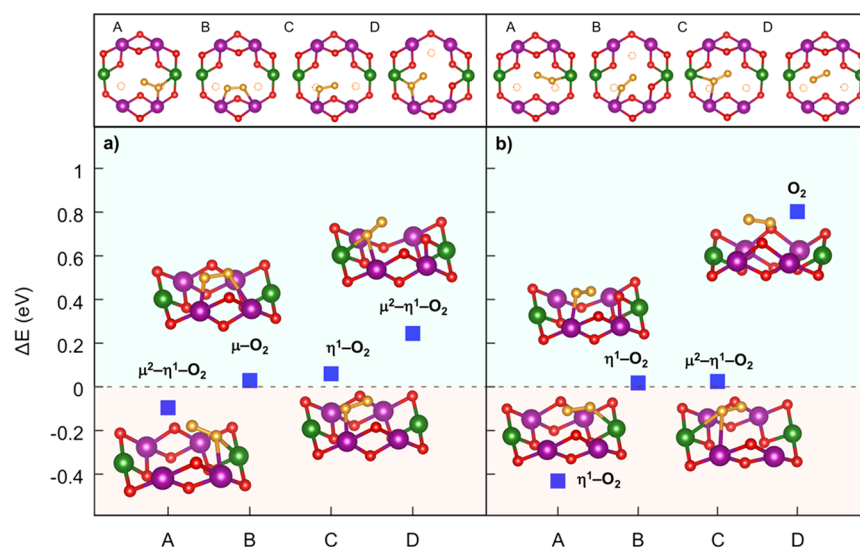
Figure 4. Dioxygen formation in NNMO: (top panel) top-view of A−D structures identified at (a) $x = 0.25$ and (b) $x = 0.125$. The yellow circles indicate the initial positions before dioxygen binding; (bottom panel) dioxygen formation energetics at (a) $x = 0.25$ and (b) $x = 0.125$. Side-views and moiety labels are also displayed according to the assignments reported in Table 2. Color code as in Figure 1, O atoms involved in the dioxygen−metal complexes are depicted in orange. Only atoms around the dioxygen complex are shown for clarity.

Table 2. O−O and M−O Distances of Dioxygen−Metal Complexes Represented in Figure 4 at $x = 0.25$ (Top) and $x = 0.125$ (Bottom) and Corresponding Assignment According to Their Coordination

x Na	O_2-intermediate	d_{O-O} (Å)	d_{M-O} (Å)	moiety	coordination
0.25	A	1.266	2.153 (Mn) - 2.272 (Ni)	$\mu^2\text{-}\eta^1\text{-}O_2$	bridging
	B	1.293	2.074 (Mn) - 2.383 (Mn)	$\mu\text{-}O_2$	binuclear bridging
	C	1.289	2.022	$\eta^1\text{-}O_2$	end-on
	D	1.263	2.281 (Mn) - 2.062 (Ni)	$\mu^2\text{-}\eta^1\text{-}O_2$	bridging
0.125	A	1.279	2.123	$\eta^1\text{-}O_2$	end-on
	B	1.288	2.155	$\eta^1\text{-}O_2$	end-on
	C	1.243	2.575 (Mn) - 2.575 (Ni)	$\mu^2\text{-}\eta^1\text{-}O_2$	bridging
	D	1.231	-	O_2	molecular O_2

vacancy formation energies are found in the p-type Mn-deficient phase than in the stoichiometric one (see Table S1 and Figures S3−S5 in SI for comparison between $Na_xNi_{0.25}Mn_{0.68}O_2$ and $Na_xNi_{0.25}Mn_{0.75}O_2$), this is consistent with the same charge compensation effect as stated in point (1). However, such effect can be less relevant when a large structural reorganization occurs upon formation of the oxygen vacancy; for example, the $V_O(2a)$ configurations in Mn-deficient phase are slightly less stable than $V_O(a)$ ones in the stoichiometric material. In these cases, the root mean squared displacement (RMSD), computed and collected in Table S2 (SI), shows a clear correlation between structural reorganization and defect formation energies. Overall, our computed E_{V_O} values are consistent with those reported for the parent layered oxide $Li_{1.2}Mn_{0.6}Ni_{0.2}O_2$.[69]

The cumulative charge variation, Δq, calculated on each element sublattice upon V_O formation is shown in Figure 3b. We have considered a threshold of $0.2e^-$ to establish a significant charge variation within a given sublattice. With this criterion, we can state that electrons left in the cell by the leaving oxygen atom are mostly host by the Mn and O sublattices, regardless of the sodiation stage (purple and red diamonds in Figure 3b), while Na and Ni sublattices are not involved in the reduction. This is particularly true when the leaving oxygen is not linked to Ni, that is V_O (1a) and V_O (2a). For the V_O (1b)-kind of vacancy, only the O sublattice is

significantly reduced at low Na contents. While the oxygen contribution to Δq is extended to the whole sublattice, reduction on manganese atoms shows a very local character (see atom-resolved contribution to charge variations in Figure S6). Actually, no differences in the overall electronic structure can be detected among the different type of V_O (see pDOS in Figure S7).

Inspired by the partial oxidation of some oxygen atoms (Figure 2e) and the facility to create an oxygen vacancy upon desodiation (Table 1), we have investigated the release of O_2 starting from the formation of dioxygen−metal compounds. Experimental evidence shows that the oxygen sublattice participates to the charge compensation mechanism upon sodium extraction only at high voltage (>4.0 V).[20] Thus, anionic redox activity should be observed in the desodiated states of such materials, enabling the chance to store extra capacity. For this reason, we have investigated the dioxygen formation only at low Na contents (>4 V state of charge) to clarify the origin of the oxygen redox processes and its underlying mechanism. Figure 4 shows the stable O_2-intermediate structures identified at $x = 0.25$ and 0.125 after relaxation and the corresponding energy variation, ΔE, given by eq 3:

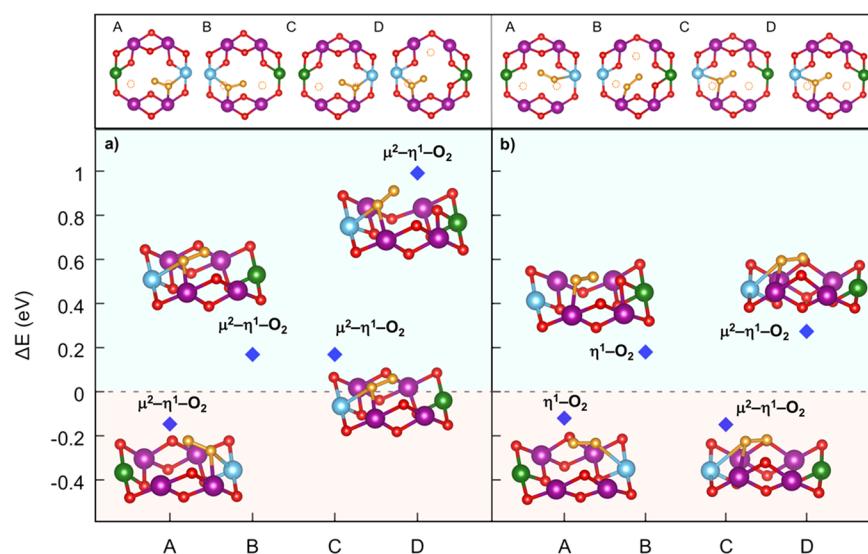$$\Delta E = E_{\text{dioxygen}} - E_{\text{NNMO}} \tag{3}$$

Figure 5. Dioxygen formation in Fe-NNMO: (top panel) top-view of A-D structures identified at (a) $x = 0.25$ and (b) $x = 0.125$; (bottom panel) dioxygen formation energetics at (a) $x = 0.25$ and (b) $x = 0.125$. Side-views and moiety labels are also displayed according to the assignments reported in Table 3. Color code as in Figure 4, plus Fe atoms depicted in light blue. Only atoms around the dioxygen complex are shown for clarity.

where $E_{dioxygen}$ is the total energy of the O_2-intermediate within NNMO lattice, and E_{NNMO} is the total energy of NNMO in its minimum-energy structure. Defined this way, negative ΔE values correspond to favorable formation of dioxygen–metal compounds from two regular O positions in the NNMO lattice. The A–D structures have been assigned to specific moieties according to M–O and O–O bond lengths and the geometry coordination, as illustrated in Table 2.

At $x = 0.25$, all the O_2-intermediate structures consist of superoxide species ($d_{O-O} \sim 1.26-1.29$ Å, intermediate between d_{O-O} in O_2 and d_{O-O} in O_2^{2-}),[70,71] which coordinate the TM in different binding modes: in A and D configurations there is a similar bridging coordination of O_2^{2-} on two adjacent Ni and Mn atoms (μ^2-η^1-O_2); B configuration involves one binuclear bridging coordination of O_2^- to contiguous Mn atoms (μ-O_2); C configuration shows an end-on coordination of O_2^{2-} on a single Mn atom (η^1-O_2). The highest formation energy is found for the μ^2-η^1-O_2 complex in D case ($\Delta E = 0.244$ eV), which is associated to an oxygen removal from the Mn–O–Mn site, while removing an oxygen atom away from a Mn–O–Ni site always results to be easier (A, B, and C cases). Among the four cases, the formation of μ^2-η^1-O_2 complex in A is the most energetically favorable ($\Delta E = -0.097$ eV), suggesting that the O-redox activity is already playing an important role at this state of charge. Since the $x = 0.25$ Na content can be assimilated to 4.1 V, this outcome explains the origin of the additional plateau exhibited during first charge cycle reported by Ma et al.[20] At $x = 0.125$, two superoxide-based complexes have been identified: both configurations A and B are assigned to end-on coordination on, respectively, a Ni and Mn atom (η^1-O_2), with structure A showing the lowest (and negative) formation energy ($\Delta E = -0.431$ eV) due to the breaking of a Ni–O bond instead of a Mn–O one compared to structure B. The C configuration, still bound but with large M-O distances, presents a near-zero formation energy and a much shorter O–O distance (1.24 Å). Beyond the formation of these dioxygen–metal complexes, such low Na content enables also the complete release of molecular oxygen: the D species features a

O–O distance of 1.23 Å and shows no direct coordination to any nearby TM atoms, with an unfavorable formation energy $\Delta E = \sim 0.8$ eV that is however easily accessible under NIB operating condition. Alike O–O peroxo-like dimers have been visualized with TEM and neutron diffraction techniques in $Li_2Ir_{1-x}Sn_xO_3$ and have been ascribed to be responsible for the capacity gain in the Li-rich layered electrode.[72] These findings prove that O-redox activity in NNMO is triggered at very low sodiation stage, i.e., high-voltage range, and that it likely occurs via formation of low-energy O_2-intermediate structures leading to the release of molecular O_2. These results have shown that Mn-bridged superoxide can form spontaneously already at x Na = 0.25 in a Mn-deficient site, while at x Na = 0.125, molecular O_2 can be easily released. However, the reversibility of this process strictly depends on what extent molecular O_2 is removed from the electrode material. Whether the oxygen molecule is trapped in the Mn-deficient site or is removed from the lattice requires further investigations. These results also clearly assess the active role of Ni in the electrochemistry of NNMO, not only in terms of the overall charge compensation upon desodiation (i.e., increasing electronic charge and decreasing magnetization upon desodiation- Figure 2b,d) but also in stabilizing dioxygen complexes. Both the Ni atom involved in the dioxygen binding and the Ni site where oxygen is removed undergo electron reduction to compensate the oxide-to-superoxide process. As shown in Figure 4, the energy difference between two similar bridged superoxide structures (i.e., A and D) can be ascribed to the different final oxygen vacancy configuration (Mn–V_O–Ni and Mn–V_O–Mn, respectively, as highlighted in top panels of Figure 4). The easier removal of one oxygen atom from a Mn–V_O–Ni site compared with the Mn–V_O–Mn (as denoted by oxygen vacancy formation energies, see Table 1) affects the final energetics of dioxygen formation, leading to the negative ΔE in A and the positive one in D. Analogously, at x Na = 0.125, the stable A structure presents a Ni–O bond and a Mn–V_O-Ni configuration, while its η^1-O_2 counterpart (i.e., the B structure without involvement of Ni) lies at higher energy.

Table 3. O−O and M−O Distances of Dioxygen−Metal Complexes in Fe-Doped NNMO represented in Figure 5 at x = 0.25 (Top) and x = 0.125 (Bottom) and Corresponding Assignment According to Their Coordination

x Na	O_2-intermediate	d_{O-O} (Å)	d_{M-O} (Å)	moiety	coordination
0.25	A	1.277	2.083 (Mn) - 2.309 (Fe)	μ^2-η^1-O_2	bridging
	B	1.299	2.010 (Mn) - 2.279 (Fe)	μ^2-η^1-O_2	bridging
	C	1.298	2.011 (Mn) - 2.297 (Fe)	μ^2-η^1-O_2	bridging
	D	1.267	2.169 (Mn) - 2.179 (Fe)	μ^2-η^1-O_2	bridging
0.125	A	1.255	2.472 (Fe)	η^1-O_2	end-on
	B	1.345	2.056 (Mn)	η^1-O_2	end-on
	C	1.265	2.445 (Mn) - 2.472 (Fe)	μ^2-η^1-O_2	bridging
	D	1.253	2.492 (Mn) - 2.606 (Fe)	μ^2-η^1-O_2	bridging

From a general perspective, the activation and control of reversible O^{2-}/O^- reactions call for fine-tuning all the constituent elements in the electrode. Increasing the TM−O bond covalency, substituting TM for d^0 or alkali metals, as well as using cation-disordered structures are among the promising strategies to suppress an irreversible O_2 loss.[34,36,39,65] Other very recent experiments also suggest that TM migration via in-plane mechanism can trigger the reversible oxygen activity with no voltage fade.[16] We have shown that Mn-deficiency is required to enable anionic redox reaction in NNMO and thus push the cathode capacity to its upper limit, but at high voltage, the labile Ni−O bond tends to release O_2 from the Mn-vacancy site via formation of low-energy superoxide intermediates. Indeed, implementing a stronger covalent nature for the TM−O bond via substitution of Ni with Fe has been recently proven to be effective: Fe-doped P2-type Na_xTMO_2 cathodes exhibit enhanced specific capacities owing to reversible O^{2-}/O^- redox and no further evolution to molecular O_2.[65] Inspired by this evidence, we have also addressed the dioxygen formation in Fe-doped NNMO in direct comparison with NNMO in order to endorse the design strategy outlined above. We consider the substitution of one Ni with one Fe atom in the Mn-deficient site (i.e., where dioxygen formation takes place), corresponding to 3% at. of metal doping, for each structure along the A−D series at both x = 0.25 and 0.125 Na contents. As illustrated in Figure 5a, at x Na = 0.25 a bridged-superoxide moiety binding to Mn and Fe atoms can form spontaneously, thus confirming that anionic activity is enabled also for Fe-NNMO at this state of charge (∼ 4.0 V).[65] Figure 5b shows that two stable structures are identified at x Na = 0.125, namely A and C, the former being end-on coordinated to Fe and the latter bridged to Fe and Mn atoms. Structural details and moiety assignments are listed in Table 3.

Different from NNMO, all the explored cases present coordinated O_2 moieties (M−O distances ranging from 2.01 to 2.61 Å) with O−O distances ascribed to superoxide-like O_2, never reaching the status of free O_2. Thus, Fe-doped NNMO is predicted to present both oxygen activity and reduced O_2 release.

As in NNMO, the energy differences among the A−D structures seem to rely on the O departure position (highlighted in top panels of Figures 4 and 5). We think that oxygen vacancy formation can also provide direct information on the tendency to form dioxygen compounds and thus be considered as correlated to the O_2 evolution. To this end, we have also computed the oxygen vacancy formation energies in Fe-doped NNMO at x Na = 0.125. Only two-coordinated $V_O(1)$-like vacancies have been considered. For three possible configurations, we obtain the following

formation energies: 2.253 eV (Mn−V_O−Mn), 1.755 eV (Mn−V_O−Fe), and 1.533 eV (Mn−V_O−Ni). These values are ∼1 eV higher than the corresponding formation energies in NNMO (1.077 eV for Mn−V_O−Mn and 0.114 eV for Mn−V_O−Ni), suggesting that Fe doping leads to an overall stabilization of the oxide lattice. On the other hand, the E_{Vo} trend found in Fe-NNMO shows that breaking the Fe−O bond is easier than the Mn−O, but more difficult than Ni−O one. The Fe−O bond is less labile than Ni−O, and it effectively allows to inhibit O_2 release in the high voltage range, but dioxygen can still form. In this way, extra specific capacity can be achieved, but it can also be recovered upon subsequent charge/discharge cycles since O_2 release is suppressed or at least reduced.

While a general picture of O-redox activity is rapidly taking shape,[37,38] our new insights on NNMO and Fe-doped NNMO highlight simple descriptors (oxygen vacancy formation and TM-O_2 coordination energy) that could allow to predict the oxygen evolution in a given structure and the critical state of charge for the irreversible material degradation.

In conclusion, we proposed a thorough first-principles investigation of the P2-type Mn-deficient $Na_xNi_{0.25}Mn_{0.68}O_2$ layered oxide, which is among the most promising candidates for an advanced high-energy NIB cathode. We focused on the anion redox activity that has been suggested by experiments[20] in order to provide new theoretical insights into the charge compensation mechanism driven by partially oxidized oxygen atoms. The O-redox process was investigated considering the formation of oxygen vacancies and dioxygen−metal species at different sodiation degrees. Accurate electronic structure analysis on NNMO revealed that desodiation is coupled to $Ni^{2+} \rightarrow Ni^{3+}$ oxidation and, when the state of charge goes up to 4.5 V, further oxidation to Ni^{4+} with a noninnocent contribution of O^{2-} takes place, while Mn^{4+} does not participate, in agreement with the available experimental observations. Increased magnetization on O atoms and p-type character of the material at x = 0.125 composition confirm that stable oxygen electron holes can be formed in NNMO at 4.5 V. Further data analysis outlined that (i) oxygen vacancies are more likely to form nearby the Mn-deficient site at low Na content (x = 0.125, i.e., 4.5 V state of charge), preferably along Mn−O−Ni bonds than along Mn−O−Mn ones; (ii) the low-energy superoxide-based structures at x = 0.25 act as possible intermediates toward the formation of molecular O_2; (iii) an oxygen molecule is expected to be released from a Mn-deficient site at x = 0.125 with preferential breaking of Ni−O bond; (iv) Fe substitution leading to increased TM−O covalency in NNMO is shown to be effective toward the stabilization of the oxide lattice and possible suppression of O_2 release. These findings set clear directions for further research

to prevent O_2 release and feature simple descriptors (oxygen vacancy formation and TM–O_2 coordination energy) that could be helpful in predicting the evolution of oxygen redox activity. Future research efforts need to focus on the effects of different TM ions on the O_2 formation mechanisms, and to chase the complete characterization of $O^{2-}/O_2^{2-}/O_2$ evolution from the bulk to the exposed surfaces. We believe that atomistic details on these processes can provide the scientific community with new rational design strategies for advanced and more efficient P2-type Na_xTMO_2 that are able to recover the extra specific capacity in subsequent charge/discharge cycles, paving the route toward the application of these promising cathode materials in high-performing Na-ion batteries.

METHODS AND COMPUTATIONAL DETAILS

We have performed spin-polarized density functional theory (DFT)[73,74] calculations with the DFT+U Hubbard-like correction scheme[75] to overcome the large self-interaction error (SIE) that affects DFT when applied to mid-to-late first-row TM oxides with tightly localized d-electrons. Projector-augmented wave (PAW) potentials and plane wave (PW) basis sets have been used, as implemented in the Vienna Ab-initio Simulation Package (VASP) code (version 5.4.4).[76] For all the calculations, the following PAW potentials[77] have been considered: Na_pv $[Be]2p^63s^1$; Ni $[Ar]3d^{10}$; Mn $[Ar]3d^7$; O $[He]2s^22p^4$. We have employed the Perdew–Burke–Ernzerhof (PBE)[78] exchange-correlation functional with U_{eff} = 4.0 eV parameter for both Ni and Mn atoms[79] and added the D3-BJ dispersion correction to account for van der Waals (vdW) interactions that play a crucial role in layered structures.[80,81] A kinetic energy of 750 eV and Γ-centered $4 \times 4 \times 4$ k-points sampling mesh have been used; these values ensure converged energies within 3 meV/f.u. with respect to the PW basis set size and Brilluoin zone sampling, respectively. For all the calculations, the convergence threshold for energy has been set to 10^{-5} eV. We have built up a $4 \times 4 \times 1$ supercell of $Na_{0.75}Ni_{0.25}Mn_{0.75}O_2$ containing 120 atoms within the $P6_3/mmc$ space group. The mixed occupancy of Ni/Mn at the 2a atomic site results in TM disorder[13,82] that can be simulated via the special quasi random structure (SQS) approach,[83,84] as implemented in the Alloy Theoretic Automated Toolkit (ATAT) code.[85,86] Na atoms have been placed in edge and face sites with Na(e)/Na(f) ratio being equal to 2 for each sodiation state.[87] Lattice constants and atomic positions for the $Na_xNi_{0.25}Mn_{0.75}O_2$ system with x = 0.125, 0.25, 0.50, 0.75 have been fully relaxed until the maximum forces acting on each atom were below 0.03 eV/Å (see Table S3 and Figures S8 and S9 in SI for details). Two Mn vacancies have been introduced in the $4 \times 4 \times 1$ supercell arranged in the most homogeneous configuration (Figure S10) to model the Mn-deficient $Na_xNi_{0.25}Mn_{0.68}O_2$ systems and further relaxation of atomic positions has been performed. No local aggregation of Mn vacancies has been reported in experiments and macroscopic samples present isotropic properties, so we considered the homogeneous configuration as best reliable model of the system. All the electronic structure calculations and geometry optimizations for O-defective and O_2-intermediate structures have been carried out within the same computational protocol. The net magnetic moment on each atom is obtained from electronic structure calculations: in case of collinear spin, VASP reports the magnetization density from the difference in the up and down spin channels, as integrated within a sphere

with a Wigner-Seitz radius for each atom type (we used the default values from VASP). Hybrid calculations with the HSE06 density functional have been performed as benchmark on selected systems as reported in the Supporting Information.

ASSOCIATED CONTENT

Ⓢⓘ Supporting Information

The Supporting Information is available free of charge at https://pubs.acs.org/doi/10.1021/acsenergylett.1c01020.

Na–O PDFs; atom-resolved contribution to charge variation and pDOS of O-defective $Na_xNi_{0.25}Mn_{0.68}O_2$; structural models and electronic features of $Na_xNi_{0.25}Mn_{0.75}O_2$ in both pristine and O-defective states; RMSD of stoichiometric and Mn-deficient phases upon oxygen vacancy formation; dioxygen formation energies computed at the HSE06 level of theory (PDF)

AUTHOR INFORMATION

Corresponding Authors

Ana B. Muñoz-García − *Department of Physics "Ettore Pancini", University of Naples Federico II, 80126 Naples, Italy; National Reference Center for Electrochemical Energy Storage (GISEL) - INSTM, 50121 Florence, Italy;* Email: anabelen.munozgarcia@unina.it

Michele Pavone − *Department of Chemical Sciences, University of Naples Federico II, 80126 Naples, Italy; National Reference Center for Electrochemical Energy Storage (GISEL) - INSTM, 50121 Florence, Italy;* ⓞ orcid.org/0000-0001-7549-631X; Email: michele.pavone@unina.it

Authors

Arianna Massaro − *Department of Chemical Sciences, University of Naples Federico II, 80126 Naples, Italy; National Reference Center for Electrochemical Energy Storage (GISEL) - INSTM, 50121 Florence, Italy;* ⓞ orcid.org/0000-0003-2950-6745

Pier Paolo Prosini − *ENEA, TERIN-PSU-ABI, C.R. Casaccia, 00123 Rome, Italy*

Claudio Gerbaldi − *Department of Applied Science and Technology (DISAT), Politecnico di Torino, 10129 Torino, Italy; National Reference Center for Electrochemical Energy Storage (GISEL) - INSTM, 50121 Florence, Italy;* ⓞ orcid.org/0000-0002-8084-0143

Complete contact information is available at:
https://pubs.acs.org/10.1021/acsenergylett.1c01020

Notes

The authors declare no competing financial interest.

Energy and Sustainable Economic Development and by Italian and European research programs. See: http://www.cresco. enea.it/english for information.

■ REFERENCES

(1) Dunn, B.; Kamath, H.; Tarascon, J.-M. Electrical Energy Storage for the Grid: A Battery of Choices. *Science (Washington, DC, U. S.)* **2011**, *334* (6058), 928−935.

(2) Larcher, D.; Tarascon, J. M. Towards Greener and More Sustainable Batteries for Electrical Energy Storage. *Nat. Chem.* **2015**, *7* (1), 19−29.

(3) Hwang, J. Y.; Myung, S. T.; Sun, Y. K. Sodium-Ion Batteries: Present and Future. *Chem. Soc. Rev.* **2017**, *46* (12), 3529−3614.

(4) Muñoz-Márquez, M. Á.; Saurel, D.; Gómez-Cámer, J. L.; Casas-Cabanas, M.; Castillo-Martínez, E.; Rojo, T. Na-Ion Batteries for Large Scale Applications: A Review on Anode Materials and Solid Electrolyte Interphase Formation. *Adv. Energy Mater.* **2017**, *7* (20), 1700463.

(5) Yoo, H. D.; Shterenberg, I.; Gofer, Y.; Gershinsky, G.; Pour, N.; Aurbach, D. Mg Rechargeable Batteries: An on-Going Challenge. *Energy Environ. Sci.* **2013**, *6* (8), 2265.

(6) Mohtadi, R.; Mizuno, F. Magnesium Batteries: Current State of the Art, Issues and Future Perspectives. *Beilstein J. Nanotechnol.* **2014**, *5* (1), 1291−1311.

(7) Yang, J.; Liu, G.; Avdeev, M.; Wan, H.; Han, F.; Shen, L.; Zou, Z.; Shi, S.; Hu, Y.-S.; Wang, C.; Yao, X. Ultrastable All-Solid-State Sodium Rechargeable Batteries. *ACS Energy Lett.* **2020**, *5* (9), 2835−2841.

(8) Zhou, C.; Bag, S.; Thangadurai, V. Engineering Materials for Progressive All-Solid-State Na Batteries. *ACS Energy Lett.* **2018**, *3* (9), 2181−2198.

(9) Abraham, K. M. How Comparable Are Sodium-Ion Batteries to Lithium-Ion Counterparts? *ACS Energy Lett.* **2020**, *5* (11), 3544−3547.

(10) Huang, Y.; Zheng, Y.; Li, X.; Adams, F.; Luo, W.; Huang, Y.; Hu, L. Electrode Materials of Sodium-Ion Batteries toward Practical Application. *ACS Energy Lett.* **2018**, *3* (7), 1604−1612.

(11) Lee, J. M.; Singh, G.; Cha, W.; Kim, S.; Yi, J.; Hwang, S.-J.; Vinu, A. Recent Advances in Developing Hybrid Materials for Sodium-Ion Battery Anodes. *ACS Energy Lett.* **2020**, *5* (6), 1939−1966.

(12) Wang, L. P.; Yu, L.; Srinivasan, M.; Xu, Z. J.; Wang, X. Recent Developments in Electrode Materials for Sodium-Ion Batteries. *J. Mater. Chem. A* **2015**, *3* (18), 9353−9378.

(13) Zhang, Y.; Zhang, R.; Huang, Y. Air-Stable Na_xTMO_2 Cathodes for Sodium Storage. *Front. Chem.* **2019**, *7*, 335.

(14) Eftekhari, A.; Kim, D.-W. Sodium-Ion Batteries: New Opportunities beyond Energy Storage by Lithium. *J. Power Sources* **2018**, *395*, 336−348.

(15) Liu, Q.; Hu, Z.; Chen, M.; Zou, C.; Jin, H.; Wang, S.; Chou, S.-L.; Dou, S.-X. Recent Progress of Layered Transition Metal Oxide Cathodes for Sodium-Ion Batteries. *Small* **2019**, *15* (32), 1805381.

(16) Wang, Q.; Mariyappan, S.; Rousse, G.; Morozov, A. V.; Porcheron, B.; Dedryvère, R.; Wu, J.; Yang, W.; Zhang, L.; Chakir, M.; Avdeev, M.; Deschamps, M.; Yu, Y.-S.; Cabana, J.; Doublet, M.-L.; Abakumov, A. M.; Tarascon, J.-M. Unlocking Anionic Redox Activity in O3-Type Sodium 3d Layered Oxides via Li Substitution. *Nat. Mater.* **2021**, *20* (3), 353−361.

(17) Delmas, C.; Fouassier, C.; Hagenmuller, P. Structural Classification and Properties of the Layered Oxides. *Physica B+C* **1980**, *99* (1), 81−85.

(18) Katcho, N. A.; Carrasco, J.; Saurel, D.; Gonzalo, E.; Han, M.; Aguesse, F.; Rojo, T. Origins of Bistability and Na Ion Mobility Difference in P2- and $O3-Na_{2/3}Fe_{2/3}Mn_{1/3}O_2$ Cathode Polymorphs. *Adv. Energy Mater.* **2017**, *7* (1), 1601477.

(19) Zhao, C.; Yao, Z.; Wang, Q.; Li, H.; Wang, J.; Liu, M.; Ganapathy, S.; Lu, Y.; Cabana, J.; Li, B.; Bai, X.; Aspuru-Guzik, A.; Wagemaker, M.; Chen, L.; Hu, Y.-S. Revealing High Na-Content P2-Type Layered Oxides as Advanced Sodium-Ion Cathodes. *J. Am. Chem. Soc.* **2020**, *142* (12), 5742−5750.

(20) Ma, C.; Alvarado, J.; Xu, J.; Clément, R. J.; Kodur, M.; Tong, W.; Grey, C. P.; Meng, Y. S. Exploring Oxygen Activity in the High Energy P2-Type $Na_{0.78}Ni_{0.23}Mn_{0.69}O_2$ Cathode Material for Na-Ion Batteries. *J. Am. Chem. Soc.* **2017**, *139* (13), 4835−4845.

(21) Mortemard de Boisse, B.; Carlier, D.; Guignard, M.; Bourgeois, L.; Delmas, C. $P2-Na_xMn_{1/2}Fe_{1/2}O_2$ Phase Used as Positive Electrode in Na Batteries: Structural Changes Induced by the Electrochemical (De)Intercalation Process. *Inorg. Chem.* **2014**, *53* (20), 11197−11205.

(22) Yabuuchi, N.; Komaba, S. Recent Research Progress on Iron- and Manganese-Based Positive Electrode Materials for Rechargeable Sodium Batteries. *Sci. Technol. Adv. Mater.* **2014**, *15* (4), 043501−043530.

(23) Talaie, E.; Duffort, V.; Smith, H. L.; Fultz, B.; Nazar, L. F. Structure of the High Voltage Phase of Layered $P2-Na_{2/3−z}[Mn_{1/2}Fe_{1/2}]O_2$ and the Positive Effect of Ni Substitution on Its Stability. *Energy Environ. Sci.* **2015**, *8* (8), 2512−2523.

(24) Somerville, J. W.; Sobkowiak, A.; Tapia-Ruiz, N.; Billaud, J.; Lozano, J. G.; House, R. A.; Gallington, L. C.; Ericsson, T.; Häggström, L.; Roberts, M. R.; Maitra, U.; Bruce, P. G. Nature of the "Z"-Phase in Layered Na-Ion Battery Cathodes. *Energy Environ. Sci.* **2019**, *12* (7), 2223−2232.

(25) Clément, R. J.; Bruce, P. G.; Grey, C. P. Review—Manganese-Based P2-Type Transition Metal Oxides as Sodium-Ion Battery Cathode Materials. *J. Electrochem. Soc.* **2015**, *162* (14), A2589−A2604.

(26) Singh, G.; Tapia-Ruiz, N.; Lopez del Amo, J. M.; Maitra, U.; Somerville, J. W.; Armstrong, A. R.; Martinez de Ilarduya, J.; Rojo, T.; Bruce, P. G. High Voltage Mg-Doped $Na_{0.67}Ni_{0.3−x}Mg_xMn_{0.7}O_2$ (x = 0.05, 0.1) Na-Ion Cathodes with Enhanced Stability and Rate Capability. *Chem. Mater.* **2016**, *28* (14), 5087−5094.

(27) Hou, P.; Sun, Y.; Li, F.; Sun, Y.; Deng, X.; Zhang, H.; Xu, X.; Zhang, L. A High Energy-Density $P2-Na_{2/3}[Ni_{0.3}Co_{0.1}Mn_{0.6}]O_2$ Cathode with Mitigated P2-O2 Transition for Sodium-Ion Batteries. *Nanoscale* **2019**, *11* (6), 2787−2794.

(28) Choi, J. U.; Jo, J. H.; Park, Y. J.; Lee, K.; Myung, S. Mn-Rich $P'2-Na_{0.67}[Ni_{0.1}Fe_{0.1}Mn_{0.8}]O_2$ as High-Energy-Density and Long-Life Cathode Material for Sodium-Ion Batteries. *Adv. Energy Mater.* **2020**, *10* (27), 2001346.

(29) Yabuuchi, N.; Kajiyama, M.; Iwatate, J.; Nishikawa, H.; Hitomi, S.; Okuyama, R.; Usui, R.; Yamada, Y.; Komaba, S. P2-Type $Na_x[Fe_{1/2}Mn_{1/2}]O_2$ Made from Earth-Abundant Elements for Rechargeable Na Batteries. *Nat. Mater.* **2012**, *11* (6), 512−517.

(30) Li, L.; Wang, H.; Han, W.; Guo, H.; Hoser, A.; Chai, Y.; Liu, X. Understanding Oxygen Redox in Cu-Doped $P2-Na_{0.67}Mn_{0.8}Fe_{0.1}Co_{0.1}O_2$ Cathode Materials for Na-Ion Batteries. *J. Electrochem. Soc.* **2018**, *165* (16), A3854−A3861.

(31) Wang, X.; Tamaru, M.; Okubo, M.; Yamada, A. Electrode Properties of $P2−Na_{2/3}Mn_yCo_{1−Y}O_2$ as Cathode Materials for Sodium-Ion Batteries. *J. Phys. Chem. C* **2013**, *117* (30), 15545−15551.

(32) Zhu, Y.-E.; Qi, X.; Chen, X.; Zhou, X.; Zhang, X.; Wei, J.; Hu, Y.; Zhou, Z. A $P2-Na_{0.67}Co_{0.5}Mn_{0.5}O_2$ Cathode Material with Excellent Rate Capability and Cycling Stability for Sodium Ion Batteries. *J. Mater. Chem. A* **2016**, *4* (28), 11103−11109.

(33) de la Llave, E.; Nayak, P. K.; Levi, E.; Penki, T. R.; Bublil, S.; Hartmann, P.; Chesneau, F.-F.; Greenstein, M.; Nazar, L. F.; Aurbach, D. Electrochemical Performance of $Na_{0.6}[Li_{0.2}Ni_{0.2}Mn_{0.6}]O_2$ Cathodes with High-Working Average Voltage for Na-Ion Batteries. *J. Mater. Chem. A* **2017**, *5* (12), 5858−5864.

(34) Zhao, C.; Yao, Z.; Wang, J.; Lu, Y.; Bai, X.; Aspuru-Guzik, A.; Chen, L.; Hu, Y.-S. Ti Substitution Facilitating Oxygen Oxidation in $Na_{2/3}Mg_{1/3}Ti_{1/6}Mn_{1/2}O_2$ Cathode. *Chem.* **2019**, *5* (11), 2913−2925.

(35) Wang, Y.; Feng, Z.; Cui, P.; Zhu, W.; Gong, Y.; Girard, M.-A.; Lajoie, G.; Trottier, J.; Zhang, Q.; Gu, L.; Wang, Y.; Zuo, W.; Yang, Y.; Goodenough, J. B.; Zaghib, K. Pillar-Beam Structures Prevent

Layered Cathode Materials from Destructive Phase Transitions. *Nat. Commun.* **2021**, *12* (1), 13.

(36) House, R. A.; Maitra, U.; Pérez-Osorio, M. A.; Lozano, J. G.; Jin, L.; Somerville, J. W.; Duda, L. C.; Nag, A.; Walters, A.; Zhou, K. J.; Roberts, M. R.; Bruce, P. G. Superstructure Control of First-Cycle Voltage Hysteresis in Oxygen-Redox Cathodes. *Nature* **2020**, *577* (7791), 502−508.

(37) Vergnet, J.; Saubanère, M.; Doublet, M.-L.; Tarascon, J.-M. The Structural Stability of P2-Layered Na-Based Electrodes during Anionic Redox. *Joule* **2020**, *4* (2), 420−434.

(38) Ben Yahia, M.; Vergnet, J.; Saubanère, M.; Doublet, M.-L. Unified Picture of Anionic Redox in Li/Na-Ion Batteries. *Nat. Mater.* **2019**, *18* (5), 496−502.

(39) Maitra, U.; House, R. A.; Somerville, J. W.; Tapia-Ruiz, N.; Lozano, J. G.; Guerrini, N.; Hao, R.; Luo, K.; Jin, L.; Pérez-Osorio, M. A.; Massel, F.; Pickup, D. M.; Ramos, S.; Lu, X.; McNally, D. E.; Chadwick, A. V.; Giustino, F.; Schmitt, T.; Duda, L. C.; Roberts, M. R.; Bruce, P. G. Oxygen Redox Chemistry without Excess Alkali-Metal Ions in $Na_{2/3}[Mg_{0.28}Mn_{0.72}]O_2$. *Nat. Chem.* **2018**, *10* (3), 288−295.

(40) Risthaus, T.; Zhou, D.; Cao, X.; He, X.; Qiu, B.; Wang, J.; Zhang, L.; Liu, Z.; Paillard, E.; Schumacher, G.; Winter, M.; Li, J. A High-Capacity P2 $Na_{2/3}Ni_{1/3}Mn_{2/3}O_2$ Cathode Material for Sodium Ion Batteries with Oxygen Activity. *J. Power Sources* **2018**, *395*, 16−24.

(41) Koga, H.; Croguennec, L.; Ménétrier, M.; Douhil, K.; Belin, S.; Bourgeois, L.; Suard, E.; Weill, F.; Delmas, C. Reversible Oxygen Participation to the Redox Processes Revealed for $Li_{1.20}Mn_{0.54}Co_{0.13}Ni_{0.13}O_2$. *J. Electrochem. Soc.* **2013**, *160* (6), A786−A792.

(42) Luo, K.; Roberts, M. R.; Hao, R.; Guerrini, N.; Pickup, D. M.; Liu, Y. S.; Edström, K.; Guo, J.; Chadwick, A. V.; Duda, L. C.; Bruce, P. G. Charge-Compensation in 3d-Transition-Metal-Oxide Intercalation Cathodes through the Generation of Localized Electron Holes on Oxygen. *Nat. Chem.* **2016**, *8* (7), 684−691.

(43) Oishi, M.; Yamanaka, K.; Watanabe, I.; Shimoda, K.; Matsunaga, T.; Arai, H.; Ukyo, Y.; Uchimoto, Y.; Ogumi, Z.; Ohta, T. Direct Observation of Reversible Oxygen Anion Redox Reaction in Li-Rich Manganese Oxide, Li_2MnO_3, Studied by Soft X-Ray Absorption Spectroscopy. *J. Mater. Chem. A* **2016**, *4* (23), 9293−9302.

(44) Sathiya, M.; Rousse, G.; Ramesha, K.; Laisa, C. P.; Vezin, H.; Sougrati, M. T.; Doublet, M. L.; Foix, D.; Gonbeau, D.; Walker, W.; Prakash, A. S.; Ben Hassine, M.; Dupont, L.; Tarascon, J. M. Reversible Anionic Redox Chemistry in High-Capacity Layered-Oxide Electrodes. *Nat. Mater.* **2013**, *12* (9), 827−835.

(45) Hong, J.; Gent, W. E.; Xiao, P.; Lim, K.; Seo, D. H.; Wu, J.; Csernica, P. M.; Takacs, C. J.; Nordlund, D.; Sun, C. J.; Stone, K. H.; Passarello, D.; Yang, W.; Prendergast, D.; Ceder, G.; Toney, M. F.; Chueh, W. C. Metal−Oxygen Decoordination Stabilizes Anion Redox in Li-Rich Oxides. *Nat. Mater.* **2019**, *18* (3), 256−265.

(46) Saubanère, M.; McCalla, E.; Tarascon, J. M.; Doublet, M. L. The Intriguing Question of Anionic Redox in High-Energy Density Cathodes for Li-Ion Batteries. *Energy Environ. Sci.* **2016**, *9* (3), 984−991.

(47) Seo, D.-H.; Lee, J.; Urban, A.; Malik, R.; Kang, S.; Ceder, G. The Structural and Chemical Origin of the Oxygen Redox Activity in Layered and Cation-Disordered Li-Excess Cathode Materials. *Nat. Chem.* **2016**, *8* (7), 692−697.

(48) Yabuuchi, N.; Nakayama, M.; Takeuchi, M.; Komaba, S.; Hashimoto, Y.; Mukai, T.; Shiiba, H.; Sato, K.; Kobayashi, Y.; Nakao, A.; Yonemura, M.; Yamanaka, K.; Mitsuhara, K.; Ohta, T. Origin of Stabilization and Destabilization in Solid-State Redox Reaction of Oxide Ions for Lithium-Ion Batteries. *Nat. Commun.* **2016**, *7* (1), 13814.

(49) Sathiya, M.; Abakumov, A. M.; Foix, D.; Rousse, G.; Ramesha, K.; Saubanère, M.; Doublet, M. L.; Vezin, H.; Laisa, C. P.; Prakash, A. S.; Gonbeau, D.; VanTendeloo, G.; Tarascon, J.-M. Origin of Voltage Decay in High-Capacity Layered Oxide Electrodes. *Nat. Mater.* **2015**, *14* (2), 230−238.

(50) Mortemard de Boisse, B.; Nishimura, S.; Watanabe, E.; Lander, L.; Tsuchimoto, A.; Kikkawa, J.; Kobayashi, E.; Asakura, D.; Okubo, M.; Yamada, A. Highly Reversible Oxygen-Redox Chemistry at 4.1 V in $Na_{4/7-x}[\square_{1/7}Mn_{6/7}]O_2$ ($\square$: Mn Vacancy). *Adv. Energy Mater.* **2018**, *8* (20), 1800409.

(51) McCalla, E.; Rowe, A. W.; Camardese, J.; Dahn, J. R. The Role of Metal Site Vacancies in Promoting Li−Mn−Ni−O Layered Solid Solutions. *Chem. Mater.* **2013**, *25* (13), 2716−2721.

(52) Mortemard De Boisse, B.; Liu, G.; Ma, J.; Nishimura, S. I.; Chung, S. C.; Kiuchi, H.; Harada, Y.; Kikkawa, J.; Kobayashi, Y.; Okubo, M.; Yamada, A. Intermediate Honeycomb Ordering to Trigger Oxygen Redox Chemistry in Layered Battery Electrode. *Nat. Commun.* **2016**, *7*, 1−9.

(53) Zhao, C.; Wang, Q.; Yao, Z.; Wang, J.; Sánchez-Lengeling, B.; Ding, F.; Qi, X.; Lu, Y.; Bai, X.; Li, B.; Li, H.; Aspuru-Guzik, A.; Huang, X.; Delmas, C.; Wagemaker, M.; Chen, L.; Hu, Y.-S. Rational Design of Layered Oxide Materials for Sodium-Ion Batteries. *Science (Washington, DC, U. S.)* **2020**, *370* (6517), 708−711.

(54) Bai, Q.; Yang, L.; Chen, H.; Mo, Y. Computational Studies of Electrode Materials in Sodium-Ion Batteries. *Adv. Energy Mater.* **2018**, *8* (17), 1702998.

(55) Zhang, X.; Zhang, Z.; Yao, S.; Chen, A.; Zhao, X.; Zhou, Z. An Effective Method to Screen Sodium-Based Layered Materials for Sodium Ion Batteries. *npj Comput. Mater.* **2018**, *4* (1), 13.

(56) Islam, M. S.; Fisher, C. A. J. Lithium and Sodium Battery Cathode Materials: Computational Insights into Voltage, Diffusion and Nanostructural Properties. *Chem. Soc. Rev.* **2014**, *43* (1), 185−204.

(57) Wang, H.; Chroneos, A.; Jiang, C.; Schwingenschlögl, U. Special Quasirandom Structures for Gadolinia-Doped Ceria and Related Materials. *Phys. Chem. Chem. Phys.* **2012**, *14* (33), 11737−11742.

(58) *High-Entropy Alloys: Fundamentals and Applications*; Gao, M. C.; Liaw, P. K.; Yeh, J. W.; Zhang, Y., Eds.; Springer, 2016.

(59) Chroneos, A.; Jiang, C.; Grimes, R. W.; Schwingenschlögl, U.; Bracht, H. E. Centers in Ternary $Si_{1-x-y}Ge_xSn_y$ Random Alloys. *Appl. Phys. Lett.* **2009**, *95* (11), 112101.

(60) Jiang, C.; Wolverton, C.; Sofo, J.; Chen, L.-Q.; Liu, Z.-K. First-Principles Study of Binary Bcc Alloys Using Special Quasirandom Structures. *Phys. Rev. B: Condens. Matter Mater. Phys.* **2004**, *69* (21), 214202.

(61) Pacchioni, G. Modeling Doped and Defective Oxides in Catalysis with Density Functional Theory Methods: Room for Improvements. *J. Chem. Phys.* **2008**, *128* (18), 182505.

(62) Lutfalla, S.; Shapovalov, V.; Bell, A. T. Calibration of the DFT/GGA+U Method for Determination of Reduction Energies for Transition and Rare Earth Metal Oxides of Ti, V, Mo, and Ce. *J. Chem. Theory Comput.* **2011**, *7* (7), 2218−2223.

(63) Wang, L.; Maxisch, T.; Ceder, G. Oxidation Energies of Transition Metal Oxides within the GGA+U Framework. *Phys. Rev. B: Condens. Matter Mater. Phys.* **2006**, *73* (19), 195107.

(64) Mosey, N. J.; Carter, E. A. Ab Initio Evaluation of Coulomb and Exchange Parameters for DFT + U Calculations. *Phys. Rev. B: Condens. Matter Mater. Phys.* **2007**, *76* (15), 155123.

(65) Zhang, Y.; Wu, M.; Ma, J.; Wei, G.; Ling, Y.; Zhang, R.; Huang, Y. Revisiting the $Na_{2/3}Ni_{1/3}Mn_{2/3}O_2$ Cathode: Oxygen Redox Chemistry and Oxygen Release Suppression. *ACS Cent. Sci.* **2020**, *6* (2), 232−240.

(66) Nakamura, T.; Ohta, K.; Kimura, Y.; Tsuruta, K.; Tamenori, Y.; Aso, R.; Yoshida, H.; Amezawa, K. Impact of Oxygen Defects on Electrochemical Processes and Charge Compensation of Li-Rich Cathode Material $Li_{1.2}Mn_{0.6}Ni_{0.2}O_{2-\delta}$. *ACS Appl. Energy Mater.* **2020**, *3* (10), 9703−9713.

(67) Muñoz-García, A. B.; Ritzmann, A. M.; Pavone, M.; Keith, J. A.; Carter, E. A. Oxygen Transport in Perovskite-Type Solid Oxide Fuel Cell Materials: Insights from Quantum Mechanics. *Acc. Chem. Res.* **2014**, *47* (11), 3340−3348.

(68) Muñoz-García, A. B.; Bugaris, D. E.; Pavone, M.; Hodges, J. P.; Huq, A.; Chen, F.; zur Loye, H.-C.; Carter, E. A. Unveiling

Structure−Property Relationships in $Sr_2Fe_{1.5}Mo_{0.5}O_{6−\delta}$, an Electrode Material for Symmetric Solid Oxide Fuel Cells. *J. Am. Chem. Soc.* **2012**, *134* (15), 6826−6833.

(69) Yan, P.; Zheng, J.; Tang, Z.-K.; Devaraj, A.; Chen, G.; Amine, K.; Zhang, J.-G.; Liu, L.-M.; Wang, C. Injection of Oxygen Vacancies in the Bulk Lattice of Layered Cathodes. *Nat. Nanotechnol.* **2019**, *14* (6), 602−608.

(70) Cramer, C. J.; Tolman, W. B.; Theopold, K. H.; Rheingold, A. L. Variable Character of O−O and M−O Bonding in Side-on (2) 1:1 Metal Complexes of O_2. *Proc. Natl. Acad. Sci. U. S. A.* **2003**, *100* (7), 3635−3640.

(71) Sutton, L. E.; Bowen, H. J. M. *Tables of Interatomic Distances and Configuration in Molecules and Ions*, Special Ed.; The Chemical Society: London, 1958.

(72) McCalla, E.; Abakumov, A. M.; Saubanere, M.; Foix, D.; Berg, E. J.; Rousse, G.; Doublet, M.-L.; Gonbeau, D.; Novak, P.; Van Tendeloo, G.; Dominko, R.; Tarascon, J.-M. Visualization of O-O Peroxo-like Dimers in High-Capacity Layered Oxides for Li-Ion Batteries. *Science (Washington, DC, U. S.)* **2015**, *350* (6267), 1516−1521.

(73) Kohn, W.; Sham, L. J. Self-Consistent Equations Including Exchange and Correlation Effects. *Phys. Rev.* **1965**, *140* (4A), A1133−A1138.

(74) Hohenberg, P.; Kohn, W. Inhomogeneous Electron Gas. *Phys. Rev.* **1964**, *136* (3B), B864−B871.

(75) Anisimov, V. I.; Zaanen, J.; Andersen, O. K. Band Theory and Mott Insulators: Hubbard U Instead of Stoner I. *Phys. Rev. B: Condens. Matter Mater. Phys.* **1991**, *44* (3), 943−954.

(76) Kresse, G.; Furthmüller, J. Efficient Iterative Schemes for Ab Initio Total-Energy Calculations Using a Plane-Wave Basis Set. *Phys. Rev. B: Condens. Matter Mater. Phys.* **1996**, *54* (16), 11169−11186.

(77) Blöchl, P. E. Projector Augmented-Wave Method. *Phys. Rev. B: Condens. Matter Mater. Phys.* **1994**, *50* (24), 17953−17979.

(78) Perdew, J. P.; Burke, K.; Ernzerhof, M. Generalized Gradient Approximation Made Simple. *Phys. Rev. Lett.* **1996**, *77* (18), 3865−3868.

(79) Tolba, S. A.; Gameel, K. M.; Ali, B. A.; Almossalami, H. A.; Allam, N. K. The DFT+U: Approaches, Accuracy, and Applications. In *Density Functional Calculations - Recent Progresses of Theory and Application*; Yang, G., Ed.; InTech, 2018; pp 3−30.

(80) Grimme, S.; Antony, J.; Ehrlich, S.; Krieg, H. A Consistent and Accurate Ab Initio Parametrization of Density Functional Dispersion Correction (DFT-D) for the 94 Elements H-Pu. *J. Chem. Phys.* **2010**, *132* (15), 154104.

(81) Barone, V.; Casarin, M.; Forrer, D.; Pavone, M.; Sambi, M.; Vittadini, A. Role and Effective Treatment of Dispersive Forces in Materials: Polyethylene and Graphite Crystals as Test Cases. *J. Comput. Chem.* **2009**, *30* (6), 934−939.

(82) Wang, Q.-C.; Meng, J.-K.; Yue, X.-Y.; Qiu, Q.-Q.; Song, Y.; Wu, X.-J.; Fu, Z.-W.; Xia, Y.-Y.; Shadike, Z.; Wu, J.; Yang, X.-Q.; Zhou, Y.-N. Tuning P2-Structured Cathode Material by Na-Site Mg Substitution for Na-Ion Batteries. *J. Am. Chem. Soc.* **2019**, *141* (2), 840−848.

(83) Zunger, A.; Wei, S.-H.; Ferreira, L. G.; Bernard, J. E. Special Quasirandom Structure. *Phys. Rev. Lett.* **1990**, *65* (3), 353−356.

(84) Mayer, J. E.; Montroll, E. *J. Chem. Phys.* **1941**, *9*, 2−16.

(85) Van de Walle, A.; Asta, M.; Ceder, G. The Alloy Theoretic Automated Toolkit: A User Guide. *CALPHAD: Comput. Coupling Phase Diagrams Thermochem.* **2002**, *26* (4), 539−553.

(86) van de Walle, A.; Sun, R.; Hong, Q.-J.; Kadkhodaei, S. Software Tools for High-Throughput CALPHAD from First-Principles Data. *CALPHAD: Comput. Coupling Phase Diagrams Thermochem.* **2017**, *58*, 70−81.

(87) Fielden, R.; Obrovac, M. N. Investigation of the $NaNi_xMn_{1-x}O_2$ ($0 \leq x \leq 1$) System for Na-Ion Battery Cathode Materials. *J. Electrochem. Soc.* **2015**, *162* (3), A453−A459.

(88) Ponti, G.; Palombi, F.; Abate, D.; Ambrosino, F.; Aprea, G.; Bastianelli, T.; Beone, F.; Bertini, R.; Bracco, G.; Caporicci, M.; Calosso, B.; Chinnici, M.; Colavincenzo, A.; Cucurullo, A.; Dangelo, P.; De Rosa, M.; De Michele, P.; Funel, A.; Furini, G.; Giammattei, D.; Giusepponi, S.; Guadagni, R.; Guarnieri, G.; Italiano, A.; Magagnino, S.; Mariano, A.; Mencuccini, G.; Mercuri, C.; Migliori, S.; Ornelli, P.; Pecoraro, S.; Perozziello, A.; Pierattini, S.; Podda, S.; Poggi, F.; Quintiliani, A.; Rocchi, A.; Scio, C.; Simoni, F.; Vita, A. The Role of Medium Size Facilities in the HPC Ecosystem: The Case of the New CRESCO4 Cluster Integrated in the ENEAGRID Infrastructure. *2014 International Conference on High Performance Computing & Simulation (HPCS)*; IEEE, 2014; pp 1030−1033.